Soft Matter

Effect of Solvent on the Emulsion and Morphology of Polyfluorene Films: All-atom molecular dynamics approach

Journal:	*Soft Matter*
Manuscript ID	SM-ART-07-2022-001001.R1
Article Type:	Paper
Date Submitted by the Author:	05-Dec-2022
Complete List of Authors:	Pinky, Sabila Kader; North Carolina State University, Materials Science and Engineering Kwansa, Albert; North Carolina State University at Raleigh, Materials Science and Engineering Zhang, Buang; Duke University, Electrical and Computer Engineering Stiff-Roberts, Adrienne; Duke University, of Electrical and Computer Engineering Yingling, Yaroslava; North Carolina State University, Materials Science and Engineering

ARTICLE

Effect of Solvent on the Emulsion and Morphology of Polyfluorene Films: All-atom molecular dynamics approach

Sabila K. Pinky[a], Albert L. Kwansa[a], Buang Zhang[b], Adrienne D. Stiff-Roberts*[b] and Yaroslava G. Yingling*[a]

The morphology of conjugated polymer thin films deposited by the resonant infrared matrix-assisted pulsed laser evaporation (RIR-MAPLE) process is related to the emulsion characteristics. However, a fundamental understanding of how and why the emulsion characteristics control the film properties and device performance is yet unclear. We performed all-atom molecular dynamics simulations of emulsions containing a mixture of polyfluorene (PFO) polymer, various primary solvents, secondary solvent, and water. The emulsion properties were then examined as a function of variable primary solvent and correlated with the morphology of deposited PFO thin films. The examination of the explicit interactions between all components of the emulsion indicated that using a primary solvent with a lower solubility-in-water and a higher non-bonded interaction energy ratio, between the solvent, polymer, and water in the emulsion recipe, produced the best result with smoother and denser films. Additionally, our simulation results are consistent with the AFM experimental results, indicating that interactions driven by trichlorobenzene (TCB) primary solvent within the emulsion are responsible for high-quality, smooth, and continuous thin film surfaces. Overall, this study can support the choice of a suitable primary solvent and provides the computational framework for predictions of new recipes for polymeric emulsion systems.

1. Introduction

Conjugated polymers are used in organic light-emitting diodes (LEDs) [1–3], solar cells [4–6], and solid-state lasers [7–9] due to their excellent optoelectronic properties. For example, polyfluorene (PF) polymers are excellent candidates for optoelectronic devices because of their wide energy band gap with a high quantum yield of photoluminescence [10–13]. Solution processing techniques such as spin casting[14], drop casting[14], and inkjet printing[15] are used typically for the preparation of these films because of their simplicity and low cost. Spin casting is probably the most popular and well-established solution processing method. Yet, devices prepared by these solution processes exhibit various solvent-induced conformational defects that are difficult to control, resulting in inconsistent device performance[16–18]. Alternatively, the resonant infrared matrix-assisted pulsed laser evaporation (RIR-MAPLE) system has been shown to exhibit better control over nanoscale morphology with the ability to deposit multi-layer films during deposition.[19–22] During RIR-MAPLE process, the polymer is dissolved in the primary solvent with low water miscibility and mixed with surfactant-containing water to make the target emulsion. A secondary solvent, phenol, is added to the emulsion to provide extra hydroxyl bonds and to lower the vapor pressure. The resultant emulsion is then frozen and irradiated with the IR laser (Er:YAG). The water phase and hydroxyl bond containing solvents resonantly absorbs the laser energy such that the frozen emulsion target sublimates, thereby transferring the emulsified polymer particles onto the substrate without degradation. Because the laser does not directly interact with the polymer, the similar polymer morphology has been observed on the substrate and in the emulsion, thereby ensuring minimal polymer morphological change between the emulsion target and deposited film. As a result, the surface roughness and internal morphology of the deposited polymer films, as well as the resultant optical and electrical properties of the films, are determined by the size and shape of the polymer clusters, or the emulsion droplet. Typically, smoother films yield better device performance.[23–25]

The size of the droplets in an emulsion depends on the composition of the emulsion, the homogenization method used, and the environmental conditions in which the emulsion was prepared.[26] Since polymers are confined within emulsion droplets, controlling droplet size is an effective way to control the surface morphology of the deposited thin film. It has been reported that droplet size and droplet size distribution play a considerable role in emulsion properties and on the deposited film morphology as well, for example, rheology, stability, texture, and appearance.[27–29] Malkin et. al.[27] studied the effect of droplet size on the rheological behavior of highly concentrated nitrite salt water-in-oil emulsions and explained how the emulsion droplet size causes dramatic changes in rheological properties such as viscosity of the emulsion system. Also, Mettu et. al.[28] have shown the influence of droplet size on the separation efficiency of mineral oil-in-water emulsions,

[a] Department of Materials Science and Engineering, North Carolina State university, Raleigh, NC 27606, USA. Email: yara_yingling@ncsu.edu
[b] Department of Electrical and Computer Engineering, Duke University, Durham, NC 27708, USA.
Electronic Supplementary Information (ESI) available.

where increasing the droplet size decreases the maximum separation efficiency. Additionally, it is also known that the morphology of the deposited films depends on the solvent used for the emulsion[30]. The choice of primary solvent can significantly affect polymer chain conformation and aggregation[25]. Moreover, the choice of primary solvent also controls emulsion properties, such as particle size, shape distribution, and transformability during solvent evaporation[31]. Thus, the selection of emulsion solvents can be used to tune the morphology and properties of deposited thin films.

All-atom molecular dynamics (MD) simulations can be used to decipher the chemical complexity of emulsions at the molecular level and provide detailed chemical and physical interactions of the emulsion mixtures. For example, atomistic MD was used to examine the surface aggregation at the oil/water interface[32] and to untangle the main mechanism of surfactants in the decane-water solution for improved oil recovery processes.[33] Previous atomistic MD simulations were able to show that in polymer-containing systems, the interactions between polymer molecules facilitate the formation of intricate elongated viscous droplets that can be related to the complex morphologies of deposited polymer films[34,35]. Although several computational studies have been performed on understanding the impact of different components involved in droplet size formation,[36–39] very few studies have been conducted on the nature of the interaction between polymers and solvents or between water and other solvents in emulsions.[40–42] Particularly, Miyamoto et al.[42] evaluated the interaction energies between all of the components present in cellulose-oil-water systems and found that cellulose can act as an emulsifying agent by coating the surface of an octane droplet. In another work, Tanis-Kanbur et al.[41] calculated interaction energies of oil-in-water emulsions with the membrane surface to see the influence of different surfactant types on membrane fouling behavior. Thus, computational approaches can be useful to untangle the role of the components influencing the emulsifying process and the development of droplet size; this will help in understanding the process-structure-property relationship for the controlled deposition of semi-crystalline polymer phase domains.

Our previous work with RIR-MAPLE has shown a correlation between the morphology of emulsions and the resultant film quality as a function of the primary solvent[43]. However, the emulsion consists of various concentrations of polymer, primary solvent, secondary solvent, surfactant, and water. Thus, a fundamental understanding of how and why the properties of the primary solvent can control the morphology of the thin film surface is still unclear. In this paper, we report on the use of all-atom MD simulations to investigate the effects of different solvents on interaction energies, how this can be correlated with experimentally measured surface roughness and quality of thin film structures, and the mechanism of the underlying reason of why different primary organic solvents affect the emulsion droplet size differently.

2. Materials and Methods

2.1. Simulation system

The emulsion mixture consists of poly(9,9-dioctylfluorene) (PFO), a variable primary solvent, phenol (PHE) as a secondary solvent, and water. All of the components were chosen to represent experimental system [43]. The secondary solvent, PHE, has a low interaction tendency towards the polymer and only helps in stabilizing the emulsion, which makes the emulsion properties largely dependent on the primary solvent. Five primary solvents were included in this study: 1,2,4-trichlorobenzene (TCB), 1,2,4-trimethylbenzene (TMB), 1,2-dichlorobenzene (DCB), toluene (TOL), and cyclopentanone (CPN). The initial 3D structures of the solvents and a PFO monomer were generated using Discovery Studio Visualizer (DSV)[44] and a 10-mer PFO polymer chain was generated using AMBER's tleap. Each system consists of ten 10-mer PFO chains that were constructed using an initial backbone dihedral angle between monomers of 165° to represent the conformation associated with the semi-crystalline form of PFO (β-PFO) [45,46]. We note that at the end of the simulations, the backbone dihedral angle distribution changed to ~80°-100° for all of the systems [Figure S1], which indicates that the PFO chains transformed into mostly amorphous phase with a very small amount of crystalline phase (β-phase). Additionally, the simulated total Hansen Solubility Parameter (HSP) for a pure 10-mer PFO polymer system was compared with the experimental value of PFO with molecular weight of 2.87 X 10^5 g mol^{-1} from Grell et. al.[47] Figure S2 shows that the simulated HSP value is lower than the experimental one due to differences in molecular weight[48,49] and formation of β-phase of the simulated polymer. It has been shows that the solubility decreases due to increase in β-phase and molecular weight.[49] The formation of β phase has a direct relationship with the chain length, hence at low molecular weight the formation of β conformation is not apparent. Moreover, the cohesive energy density and solubility decrease with the increase in molecular weight.[50]

The polymer chains, primary solvent, secondary solvent, and water were placed randomly in a computational box of dimensions 200 x 200 x 200 $Å^3$ using the Packmol software [51]. Surfactants were omitted in this study due to the low concentration of surfactants in experiments (e.g., 0.001 wt%), which would result in a negligible number of surfactant molecules in the simulation box. A solvent ratio of 1:0.25:3 (primary solvent : secondary solvent : water) was employed to represent the emulsion recipe. The details of the simulation systems including the total number of atoms, mass fraction, and number of each chemical species are presented in Table S1. All systems has the same mass fraction of PFO, PS, SS, and WAT, which are 0.5, 0.118, 0.029, and 0.353 respectively. Hence, our simulation systems have a total number of atoms ranging from 12,391 to 13,667. The influence of system size in MD simulations has been studied earlier.[52–54] For example, Neyertz and Brown[53] performed MD simulations of gas diffusion in the glassy polymer ODPA-ODA with different box sizes. They predicted the average densities, intermolecular energies, Hildebrand parameters, mean square radii of gyration, radial distribution functions, and solubilities for the 4,150-atom,

6,225-atom, and 56,025-atom pure matrices. However, by increasing the model size, the accuracy of the predictions was not necessarily improved. Although there are different numbers of atoms in the systems, yet all the models remain consistent with each other. Additionally, in this study, we did not address the morphology of the emulsion since we ignored the addition of surfactants. Our simulation systems are not large enough to conclude about the morphology accurately, but large enough to predict properties like density, solubility, radial distribution functions, and intermolecular energies. For investigating the morphology of emulsion systems, mesoscale modeling, i.e., coarse-grained (CG) MD simulation is mostly used.[55–57] Fig. 1 shows the schematic view of the emulsion system and displays the molecular structures of the emulsion components. A representative snapshot of the simulation system after energy minimization is also presented in Fig. 1F.

2.2. Molecular Dynamics Simulation

All-atom molecular dynamics (MD) simulations were performed following the protocols developed by Taylor et al.[58], and Allen et al.[59] The AMBER 2018[60] software package was used for the simulations using the General AMBER Force Field (GAFF2)[61,62], TIP3P water model[63], and Joung-Cheatham monovalent ion parameters for TIP3P[64].

Atomic partial charges for the primary solvents, secondary solvent, and PFO monomer were calculated using Gaussian 16[65] and fitted with the Restrained Electrostatic Potential (RESP) method and RESP-A1 charge model[66] via R.E.D. Server Development[67]. The resultant time-averaged density, dipole moment, and total Hansen Solubility Parameter for the primary solvents are listed in Table S2, and all the partial charges for each component are listed in Table S3. It is noteworthy that some of the hydrogen atoms in the PFO polymer have negative charge. While assigning partial charges via R.E.D. Server Development, these charges were optimized to reproduce the electrostatic potential (ESP) quantum mechanics (QM) data. The statistics of the fitting for the end fragment and middle fragment of the PFO polymer are given in Table S4. From the statistics of the fitting, the root-mean-square (RMS) errors and relative RMS (RRMS) errors are low at ~0.0019 and ~0.28, respectively, which means that the difference between the calculated ESP and QM ESP data is relatively small and demonstrates the quality of these charges. For instance, RMS errors ranging individually from ~0.01 to ~0.1 and on average from 0.0139 to 0.0277 have been reported for three training sets including 45 compounds using RESP fitting[11]. Also, RRMS errors ranging from 0.0143 to 0.8627 have been reported for four compounds using RESP fitting[11]. These slightly negative partial charges for some hydrogen atoms were obtained only for the non-polar aliphatic tail groups of the PFO units where the partial charges (carbon and hydrogen) are very weak; such weak negative partial charges for hydrogen atoms have been previously reported with RESP fitting[12]. Additionally, the squared correlation coefficient (or coefficient of determination), R^2, for both fragments is relatively high > 0.90. While calculating the partial charges, there was no restraint on the sign of the charges, allowing weak charges for hydrogen atoms such as these to be negative if this improves the overall quality of the charges (e.g., lower RMS, lower RRMS, and higher R^2). Moreover, these negative charges on some hydrogen atoms are less than -0.005 e^- and are linked to carbons also with weak partial charges near zero, assuring that these negative partially charged hydrogen atoms have no other effects.

The choice of GAFF2 force field was validated using experimental densities and solubility parameters. The discrepancies between simulated and experimental densities and total Hansen Solubility Parameter (HSP) values are small for all of the solvents (1.73% and 2.9%, respectively) (Figure S3).

A system was subjected to minimization and equilibration protocols prior to the production simulations. Energy minimization was performed for up to 100,000 steps using the steepest descent method for 10 steps, followed by the conjugate gradient method for remaining steps. The systems were then gradually heated to 300 K (100-ps ramp, 50-ps hold), equilibrated using a 1-ns NVT run at 300 K and then a 10-ns NPT run at 300 K and 1 atm. Production simulation using NPT was performed for 50 ns with a 2-fs timestep; the pressure was regulated isotropically using the Monte Carlo barostat (changes attempted every 100 steps), and the Berendsen thermostat was used to maintain the system temperature (τ = 1 ps). All simulations used an 8.0-Å cut-off for non-bonded interactions, and the SHAKE algorithm was used for bonds with hydrogen atoms. The particle-mesh Ewald (PME)[64] method and Lennard-Jones correction[60] were used for long-range interactions.

The analysis of dihedral angles, radial distribution functions (RDFs), and non-bonded interaction energies (Coulombic and Lennard-Jones) were performed using AMBER's cpptraj "lie" action from AmberTools 21[68]. The non-bonded interaction energies were calculated between all atoms of all primary solvent molecules (selection 1) and all atoms of all polymer molecules (selection 2) for the primary solvent-polymer pair. A similar approach was taken for the primary solvent-water pair. Both the Coulombic (electrostatic) energy and 12-6 Lennard-Jones energy (includes van der Waals attraction) were calculated for each frame, and the average was calculated over all of the frames. These interaction energies were calculated while accounting for periodic boundary conditions to represent bulk interaction energies. The RDF calculation was done using the histogram of the number of particles found within radial distance bins with a bin width of 0.1 Å. For RDF normalization, a default density was used corresponding to that of water, which was 0.033456 molecules/Å^3. While calculating the non-bonded interaction energies, a 12-Å cut-off distance was used.

2.3 Experimental materials and methods

The experimental procedure was performed using the resonant infrared matrix-assisted pulsed laser evaporation (RIR-MAPLE) system. In order to make the target emulsion, PFO was dissolved in the primary solvent with low water miscibility and mixed with surfactant-containing water. The polymer and primary solvent, then, gets dispersed as droplets into the continuous water phase to form an oil-in-water (O/W) emulsion. The solvent droplet size depends on the surfactant. Finally, a secondary solvent, phenol, is added to the emulsion to

provide extra hydroxyl bonds and to lower the vapor pressure. The resultant emulsion after vigorous shaking is injected into the deposition target cup which is pre-cooled by liquid nitrogen to -196^{0}C, and flash-frozen into a solid target such that the polymer clusters are maintained. The RIR-MAPLE system uses an IR laser (Er:YAG) with a peak wavelength of 2.94 μm, which is resonant with the vibrational modes of hydroxyl bonds within the matrix of the emulsion target (ice). Atomic force microscopy (AFM) images were obtained using a Dimension 3100 system in tapping mode, while images were analyzed for root-mean-square (RMS) surface roughness and film thickness using the Gwyddion software[69].

3. Results and Discussion

The experimental results indicated that the primary solvents solubility in water is the main property responsible for the emulsion properties and stability[43]. To decipher the underlying mechanism for this observation, we analyzed the interactions between the solvents and water. Here, Figure 2(A) shows the radial distribution function (RDF) between water and primary solvents. We observed that the RDF between water-solvent is the highest for CPN and the lowest for TCB, with an ascending order from TCB, TMB, DCB, TOL, and CPN. The RDF profiles are directly related to calculations of non-bonded interaction energy (Figure 2B), where TCB has the lowest interaction energy with water, and CPN has the highest interaction energy with water; other solvents also maintain the same order as the RDFs. Thus, the solubility-in-water of primary solvents follows an ascending order of TCB, TMB, DCB, TOL, and CPN. However, when a solvent has very low solubility in water, it will be repelled by the water and will be attracted towards other components, preferably polymer, to form a smaller dispersed droplet. Figures 2(C) and 2(D) show the RDF and non-bonded interaction energy between the polymer and primary solvent, respectively; these results show that all primary solvents tend to interact with the polymer more than with water, except for CPN. CPN's interaction tendency toward water can be attributed to its carbonyl group and hydrogen bond propensity, i.e., CPN is the only primary solvent in this set with a hydrogen bond acceptor or donor [Figure 1(B)].

We found experimentally that a lower solubility-in-water is associated with smoother, denser films, and the simulation revealed that these emulsions comprised of compact, spherical droplets[23]. Previous dissipative particle dynamics (DPD) also showed that lower solubility-in-water leads to the smaller droplet size[23]. The atomic force microscopy (AFM) analysis [Figure 3(A)] and surface profile [Figure 3(B)] of deposited thin films for all five primary solvents (Table S5) show a very good agreement between experimental and simulated observations. The surface morphology of the thin films appears as peaks and valleys resulting from the polymer clusters deposited on the substrate. It is clearly spotted that the surface roughness, with mean roughness values (R_a) increasing from 12.63 nm for the thin film sample deposited with TCB [Figure 3(A)] to an R_a value of 291.0 nm for the roughest film deposited with CPN. As shown in the AFM images in Figure 3(A), using TCB yielded the smoothest film surface representing the smallest droplet size during deposition, while using CPN yielded the roughest film surface with large polymer aggregates. The surface profile confirms the shifts from a flat surface to a more roughened surface as the polymer aggregation size increases [Figure 3(B)]. AFM line profiles of each of the samples shows the dependency of the surface morphology on different solvents. In addition, Table S3 shows a trend from TCB to CPN where the values of solubility-in-water and film roughness are increasing with a decrease of the interaction energy ratio between polymer to primary solvent and primary solvent to water.

The solubility-in-water of organic solvents is directly related to the bonding between solvent and water molecules. We hypothesize that the relative bonding energy between solvent-polymer and solvent-water determines the emulsion droplet size. To examine this hypothesis, we plotted primary solvent-water (PS-WAT) interaction energy obtained from simulations versus PS solubility in water measured experimentally [43] in Figure 4(A) and observed an inverse relation, which is expected and indicative of good agreement between simulations and experiment. Since the emulsion properties and the deposited film properties should be interrelated, we then compared the emulsion interaction energy ratio (PS-polymer to PS-water) to film surface roughness obtained from AFM [Figure 4(B)], which shows that the roughness of the film surface increases with the decrease in the emulsion interaction energy ratio. From Figure 4, we can observe that the decrease of the PS solubility-in-water parameter will lead to the decrease in the surface roughness of the film. However, a low interaction energy between PS and water could lead to a higher emulsion interaction energy ratio. PS with a high emulsion interaction energy ratio means the primary solvent molecules are more attracted to the polymer than water. We reason that this higher attraction between PS and polymer will lead to the formation of a densely packed polymer cluster inside the droplet, which will be transferred in the substrate during deposition, resulting in a smoother film surface. Additionally, emulsion droplets in the water generally tend to merge with each other upon contact, leading to a larger droplet size. Therefore, less attraction between primary solvent and water molecules will confirm the discrete suspension of smaller droplets in the water with less coalescence during the deposition.

In this scenario, TCB has a greater bonding propensity to PFO molecules than to water, due to the very low solubility-in-water of TCB (PS-PFO:PS-WAT energy ratio of 7.537). PFO and water molecules attract and repel TCB droplets, respectively, preventing coalescence and ensuring strong water dispersion. Because of the water dispersion, the emulsion droplets are suspended in water, which prevents two droplets from merging with each other during contact that can produce a larger droplet size. When TOL is used as the primary solvent, however, the solvent droplets coalesce easily inside the emulsion. Since the bonding strength of TOL molecules to water molecules is far less than the bonding strength of TOL molecules to PFO molecules (PS-PFO:PS-WAT energy ratio of 3.037), a poor emulsion results in such a situation because of the partial miscibility of TOL in

water as shown by its higher solubility-in-water. Hence, larger clusters arise from the large number of polymer molecules bonding with available TOL molecules. In contrast, the polymer is directly precipitated from the solution as bulk solid particles when used as the main resolver to produce an emulsion. This phenomenon of polymer precipitation happens because of the high solubility-in-water of CPN, which confirms the stronger interaction strength of CPN molecules to water molecules compared to the interaction strength of CPN molecules to PFO molecules (PS-PFO:PS-WAT energy ratio of 0.510). The CPN molecules' direct interaction with water molecules exposes the PFO molecules to an abundance of water, causing the PFO molecules to precipitate due to their poor miscibility with water.[23]

However, TMB is the only solvent that does not follow the previously mentioned trend. Though TMB has a lower solubility-in-water than DCB, the film surface roughness is comparatively higher when TMB is used as a primary solvent versus DCB. Previously, we concluded that the stronger the interaction strength between solvents and polymer molecules, relative to the interaction strength between solvent molecules and water molecules, the smaller the organic solvent droplet is in the corresponding emulsion. This competition between two interaction strengths is significant because it explains why TMB films, considering their low water solubility, are not smooth. This can also be explained by TMB's heavy side chain and comparatively higher vapor pressure than DCB.[23,70]

4. Conclusions

The correlation between primary solvent properties and interactions with other constituents in emulsions and the properties of conjugated polymer thin films were examined. We investigated explicit interactions formed between primary solvents and other emulsion components, e.g., primary solvents' solubility-in-water, interaction energy between primary solvent and all other components, etc. We found that the solubility of primary solvent in water determines the emulsion droplet size, and a lower solubility in water produces smaller and denser droplets that yield a smoother and denser film surface. In addition, a high non-bonded interaction energy of the primary solvent with the polymer is useful for the deposition of high-quality surfaces. The higher the ratio of the interaction energy of the primary solvent with the polymer and primary solvent with the water, the smoother the film surface. The AFM characterization also shows a very good agreement with simulation-based observations.

This study presented that the emulsion prepared using trichlorobenzene (TCB) produced the smoothest film surface representing the smallest droplet size while having the lowest solubility-in-water value, and highest interaction energy with polymer as well. However, using cyclopentanone (CPN) produced the roughest film surface with the largest polymer aggregates that has the highest solubility-in-water value compared to the other primary solvents, and a very low interaction energy with the polymer. Moreover, this study also presents a trend from TCB to CPN where the values of solubility-in-water and film roughness are increasing with a decrease of the interaction energy ratio between the polymer to primary solvent and the primary solvent to water. Our study indicates that the identity of the solvents in emulsion mixtures is critically important, and the judicious selection of a mixture affords some level of control over the film surface prior to the deposition of thin films. Therefore, the conclusions of this study provide an atomic-level insight into the reason behind different surface morphologies, and proposed strategies for using the most suitable type of primary solvent to control thin film properties in polymeric-based materials.

Author Contributions

A.D.S.R, Y.G.Y. designed research; S.K.P. performed simulation studies; B.Z. performed experimental studies; S.K.P., B.Z., A.L.K. analyzed data; and S.K.P, B.Z., A.L.K., A.D.S.R., Y.G.Y. wrote the paper.

Conflicts of interest

There are no conflicts to declare.

Acknowledgements

This study was supported by the National Science Foundation CMMI-1727572.

References

1 J. Peet, E. Brocker, Y. Xu and G. C. Bazan, *Adv. Mater.*, 2008, **20**, 1882–1885.
2 F.-I. Wu, P.-I. Shih, C.-F. Shu, Y.-L. Tung and Y. Chi, *Macromolecules*, 2005, **38**, 9028–9036.
3 Y. Fang, E. Gu, L. Chi, R. Xia, W. Huang, Q. Zhang, G. Hai and X. Li, *Molecules*, 2017, **22**, 315.
4 H.-Y. Chen, J. Hou, S. Zhang, Y. Liang, G. Yang, Y. Yang, L. Yu, Y. Wu and G. Li, *Nat. Photonics*, 2009, **3**, 649–653.
5 S. Günes, H. Neugebauer and N. S. Sariciftci, *Chem. Rev.*, 2007, **107**, 1324–1338.
6 K. W. Chou, B. Yan, R. Li, E. Q. Li, K. Zhao, D. H. Anjum, S. Alvarez, R. Gassaway, A. Biocca, S. T. Thoroddsen and others, *Adv. Mater.*, 2013, **25**, 1923–1929.
7 J.-Y. Lin, W.-S. Zhu, F. Liu, L.-H. Xie, L. Zhang, R. Xia, G.-C. Xing and W. Huang, *Macromolecules*, 2014, **47**, 1001–1007.
8 D. Schneider, T. Rabe, T. Riedl, T. Dobbertin, O. Werner, M. Kröger, E. Becker, H.-H. Johannes, W. Kowalsky, T. Weimann and others, *Appl. Phys. Lett.*, 2004, **84**, 4693–4695.
9 H. Wang, F. Li, B. Gao, Z. Xie, S. Liu, C. Wang, D. Hu, F. Shen, Y. Xu, H. Shang and others, *Cryst. Growth Des.*, 2009, **9**, 4945–4950.
10 B. Zhu, Y. Han, M. Sun and Z. Bo, *Macromolecules*, 2007, **40**, 4494–4500.
11 J. Teetsov and M. A. Fox, *J. Mater. Chem.*, 1999, **9**, 2117–2122.

12 J. Liang, L. Yu, S. Zhao, L. Ying, F. Liu, W. Yang, J. Peng and Y. Cao, *Nanotechnology*, 2016, **27**, 284001.
13 H. H. Lu, C. Y. Liu, C. H. Chang and S. A. Chen, *Adv. Mater.*, 2007, **19**, 2574–2579.
14 J. Danglad-Flores, S. Eickelmann and H. Riegler, *Chem. Eng. Sci.*, 2018, **179**, 257–264.
15 H. Sirringhaus, T. Kawase, R. H. Friend, T. Shimoda, M. Inbasekaran, W. Wu and E. P. Woo, *Science (80-.).*, 2000, **290**, 2123–2126.
16 Y. Xie, S. Gao and M. Eslamian, *Coatings*, 2015, **5**, 488–510.
17 M. Eslamian, *Coatings*, 2014, **4**, 60–84.
18 D. P. Birnie III, *Langmuir*, 2013, **29**, 9072–9078.
19 Y. S. and Z. J, *Front Nanosci Nanotech 3*, , DOI:10.15761/FNN.1000146.
20 B. Toftmann, M. R. Papantonakis, R. C. Y. Auyeung, W. Kim, S. M. O'Malley, D. M. Bubb, J. S. Horwitz, J. Schou, P. M. Johansen and R. F. Haglund, *Thin Solid Films*, 2004, **453–454**, 177–181.
21 A. D. Stiff-Roberts and W. Ge, *Appl. Phys. Rev.*, 2017, **4**, 41303.
22 A. P. Caricato, W. Ge and A. D. Stiff-Roberts, in *Advances in the application of lasers in materials science*, Springer, 2018, pp. 275–308.
23 W. Ge, N. K. Li, R. D. McCormick, E. Lichtenberg, Y. G. Yingling and A. D. Stiff-Roberts, *ACS Appl. Mater. Interfaces*, 2016, **8**, 19494–19506.
24 K. R. Lantz, R. Pate, A. D. Stiff-Roberts, A. G. Duffell, E. R. Smith and H. O. Everitt, *J. Vac. Sci. Technol. B Microelectron. Nanom. Struct. Process. Meas. Phenom.*, 2009, **27**, 2227–2231.
25 B. J. Schwartz, *Annu. Rev. Phys. Chem.*, 2003, **54**, 141–172.
26 S. Kanafusa, B.-S. Chu and M. Nakajima, *Eur. J. lipid Sci. Technol.*, 2007, **109**, 1038–1041.
27 A. Y. Malkin, I. Masalova, P. Slatter and K. Wilson, *Rheol. Acta*, 2004, **43**, 584–591.
28 S. Mettu, S. Yao, Q. Sun, S. R. Lawson, P. J. Scales, G. J. O. Martin and M. Ashokkumar, *Ind. Eng. Chem. Res.*, 2020, **59**, 7901–7912.
29 R. Pal, *AIChE J.*, 1996, **42**, 3181–3190.
30 P. Müller-Buschbaum, J. S. Gutmann, M. Wolkenhauer, J. Kraus, M. Stamm, D. Smilgies and W. Petry, *Macromolecules*, 2001, **34**, 1369–1375.
31 Muhaimin and R. Bodmeier, *Polym. Int.*, 2017, **66**, 1448–1455.
32 P. Shi, H. Zhang, L. Lin, C. Song, Q. Chen and Z. Li, *J. Dispers. Sci. Technol.*, 2018, **39**, 1758–1766.
33 L. S. de Lara, M. F. Michelon and C. R. Miranda, *J. Phys. Chem. B*, 2012, **116**, 14667–14676.
34 Y. Cheng and S. Yuan, *Molecules*, 2020, **25**, 3008.
35 X. Liu, Y. Li, S. Tian and H. Yan, *J. Phys. Chem. C*, 2019, **123**, 25246–25254.
36 K. K. Lee, D. Y. Low, M. L. Foo, L. J. Yu, T. S. Choong, S. Y. Tang and K. W. Tan, *Polym.* , 2021, 13.
37 J. Ma, X. Song, J. Luo, T. Zhao, H. Yu, B. Peng and S. Zhao, *Langmuir*, 2019, **35**, 13636–13645.
38 T. Ma, X. Hu, S. Lu, R. Cui, J. Zhao, X. Hu and Y. Song, *Int. J. Biol. Macromol.*, 2021, **184**, 405–414.
39 N. K. Li, W. H. Fuss, L. Tang, R. Gu, A. Chilkoti, S. Zauscher and Y. G. Yingling, *Soft Matter*, 2015, **11**, 8236–8245.
40 M. Darvishi and M. Foroutan, *RSC Adv.*, 2016, **6**, 74124–74134.
41 M. B. Tanis-Kanbur, S. Velioğlu, H. J. Tanudjaja, X. Hu and J. W. Chew, *J. Memb. Sci.*, 2018, **566**, 140–150.
42 H. Miyamoto, D. M. Rein, K. Ueda, C. Yamane and Y. Cohen, *Cellulose*, 2017, **24**, 2699–2711.
43 S. Ferguson, C. V. Williams, B. Mohapi and A. D. Stiff-Roberts, *J. Electron. Mater.*, 2019, **48**, 3388–3398.
44 D. Studio, *Accelrys [2.1]*.
45 Y.-D. Liu, Q. Zhang, X.-H. Yu, J.-G. Liu and Y.-C. Han, *Chinese J. Polym. Sci.*, 2019, **37**, 664–673.
46 L. Huang, X. Huang, G. Sun, C. Gu, D. Lu and Y. Ma, *J. Phys. Chem. C*, 2012, **116**, 7993–7999.
47 M. Grell, D. D. C. Bradley, X. Long, T. Chamberlain, M. Inbasekaran, E. P. Woo and M. Soliman, *Acta Polym.*, 1998, **49**, 439–444.
48 M. M. Abdelghafour, Á. Orbán, Á. Deák, Ł. Lamch, É. Frank, R. Nagy, A. Ádám, P. Sipos, E. Farkas, F. Bari and L. Janovák, *Polymers (Basel).*, 2021, 13.
49 T. Li, Q. He, Y. Guan, J. Liao, Y. He, X. Luo, W. Cao, Z. Cui, S. Jia, A. Liu, S. Yao, X. Guan, H. Zhang and D. Lu, *Polymer (Guildf).*, 2022, **240**, 124471.
50 C. Li and A. Strachan, *Polymer*, 2018, 135, 162-170.
51 L. Martínez, R. Andrade, E. G. Birgin and J. M. Martínez, *J. Comput. Chem.*, 2009, **30**, 2157–2164.
52 A. Mahata and M. Asle Zaeem, *Model. Simul. Mater. Sci. Eng.*, 2019, **27**, 85015.
53 S. Neyertz and D. Brown, *Macromolecules*, 2004, **37**, 10109–10122.
54 B. Dünweg and K. Kremer, *J. Chem. Phys.*, 1993, **99**, 6983–6997.
55 V. V Ginzburg, *Ind. Eng. Chem. Res.*
56 X.-L. Sun, S.-S. Li, Z.-B. Liu, P. Wang, S. Pei and J. Zhang, *Colloids Surfaces A Physicochem. Eng. Asp.*, 2017, **533**, 140–146.
57 T. Duran, A. Costa, A. Gupta, X. Xu, H. Zhang, D. Burgess and B. Chaudhuri, *Mol. Pharm.*, 2022, **19**, 1117–1134.
58 N. G. Taylor, S. H. Chung, A. L. Kwansa, R. R. Johnson III, A. J. Teator, N. J. B. Milliken, K. M. Koshlap, Y. G. Yingling, Y. Z. Lee and F. A. Leibfarth, *Chem. – A Eur. J.*, 2020, **26**, 9982–9990.
59 B. P. Allen, Z. M. Wright, H. F. Taylor, T. J. Oweida, S. Kader-Pinky, E. F. Patteson, K. M. Bucci, C. A. Cox, A. S. Senthilvel, Y. G. Yingling and A. S. Knight, *Angew. Chemie Int. Ed.*, 2022, **61**, e202115547.
60 D. A. Case, I. Y. Ben-Shalom, S. R. Brozell, D. S. Cerutti, T. E. Cheatham III, V. W. D. Cruzeiro, T. A. Darden, R. E. Duke, D. Ghoreishi and M. K. Gilson, *Univ. California, San Fr.*
61 D. Vassetti, M. Pagliai and P. Procacci, *J. Chem. Theory Comput.*, 2019, **15**, 1983–1995.
62 J. Wang, R. M. Wolf, J. W. Caldwell, P. A. Kollman and D. A. Case, *J. Comput. Chem.*, 2004, **25**, 1157–1174.
63 W. L. Jorgensen, J. Chandrasekhar, J. D. Madura, R. W. Impey and M. L. Klein, *J Chem Phys*, 1983, **79**, 926–935.
64 I. S. Joung and T. E. Cheatham III, *J. Phys. Chem. B*, 2008,

112, 9020–9041.
65 M. J. Frisch, G. W. Trucks, H. B. Schlegel, G. E. Scuseria, M. A. Robb, J. R. Cheeseman, G. Scalmani, V. Barone, G. A. Petersson and H. Nakatsuji, 2016.
66 C. I. Bayly, P. Cieplak, W. Cornell and P. A. Kollman, *J. Phys. Chem.*, 1993, **97**, 10269–10280.
67 E. Vanquelef, S. Simon, G. Marquant, E. Garcia, G. Klimerak, J. C. Delepine, P. Cieplak and F.-Y. Dupradeau, *Nucleic Acids Res.*, 2011, **39**, W511–W517.
68 A. Case, H. M. Aktulga, K. Belfon, I. Y. Ben-Shalom, S. R. Brozell, D. S. Cerutti, T. E. Cheatham III, G. A. Cisneros, V. W. D. Cruzeiro and T. A. Darden, .
69 D. Nečas and P. Klapetek, *Open Phys.*, 2012, **10**, 181–188.
70 M. Xiao, J. Jasensky, X. Zhang, Y. Li, C. Pichan, X. Lu and Z. Chen, *Phys. Chem. Chem. Phys.*, 2016, **18**, 22089–22099.

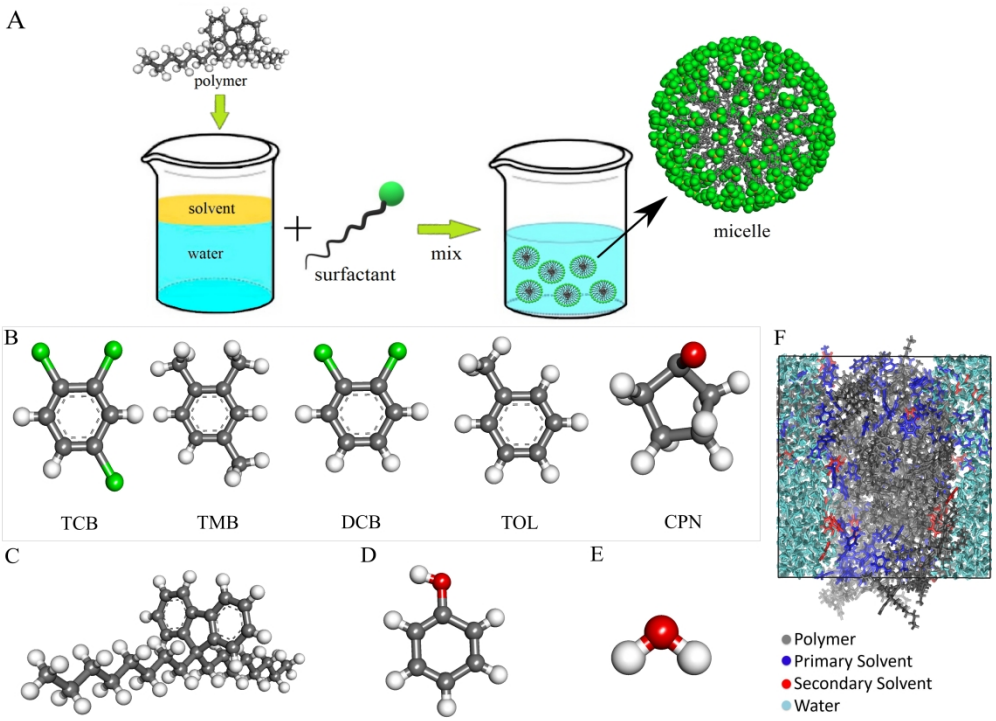

Figure 1 (A) Schematic view of the emulsion mixture. Molecular structure of (B) all primary solvents [1,2,4-trichlorobenzene (TCB), 1,2,4-trimethylbenzene (TMB), 1,2-dichlorobenzene (DCB), toluene (TOL), cyclopentanone (CPN)], (C) polymer monomer (PFO), (D) secondary solvents [phenol (PHE)] , (E) water, and (F) Representative configuration of the simulation model with primary solvent TCB after energy minimization.White, gray, green, and red color represent hydrogen, carbon, chlorine, and oxygen atoms, respectively.

529x393mm (236 x 236 DPI)

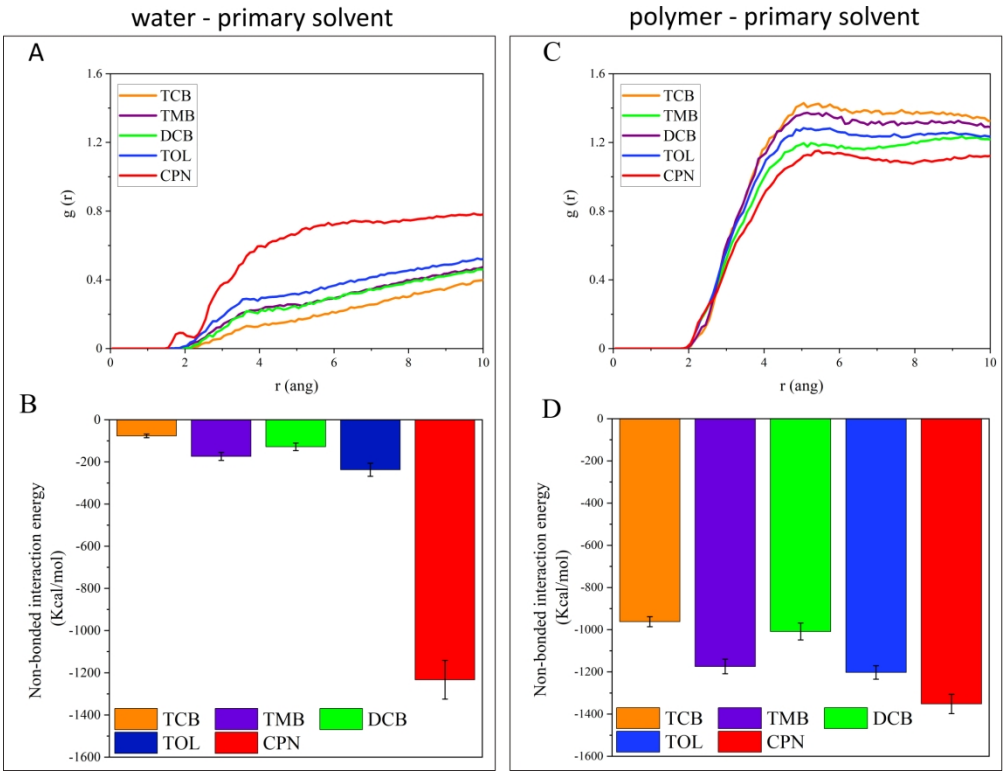

Figure 2 (A) Radial distribution functions for water and primary solvent (B) non-bonded interaction energy between water and primary solvent, (C) Radial distribution functions for polymer and primary solvent, and (D) non-bonded interaction energy between polymer and primary solvent.

248x189mm (236 x 236 DPI)

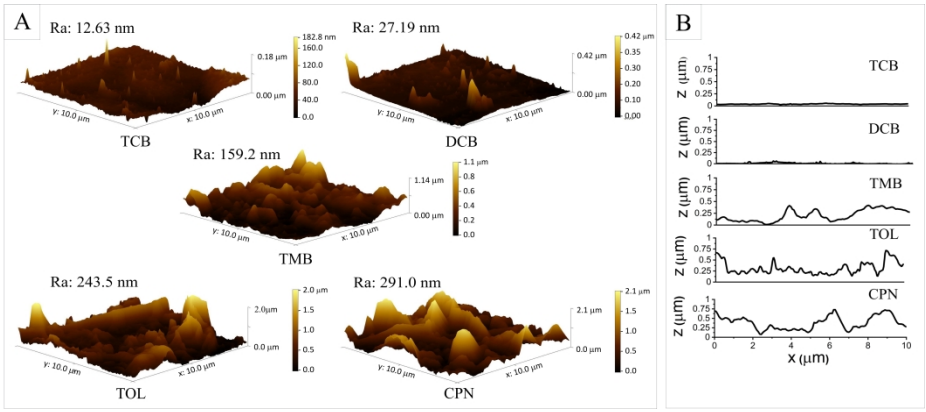

Figure 3 (A) AFM images and (B) surface profile of thin films deposited with different primary solvents using the RIR-MAPLE technique. Ra indicates the mean surface roughness; calculated on 10x10 µm^2 regions. The gradient scale bar for each AFM figure has a different scale. Images are taken from the experimental work done by Ferguson et. al. [43]

586x238mm (236 x 236 DPI)

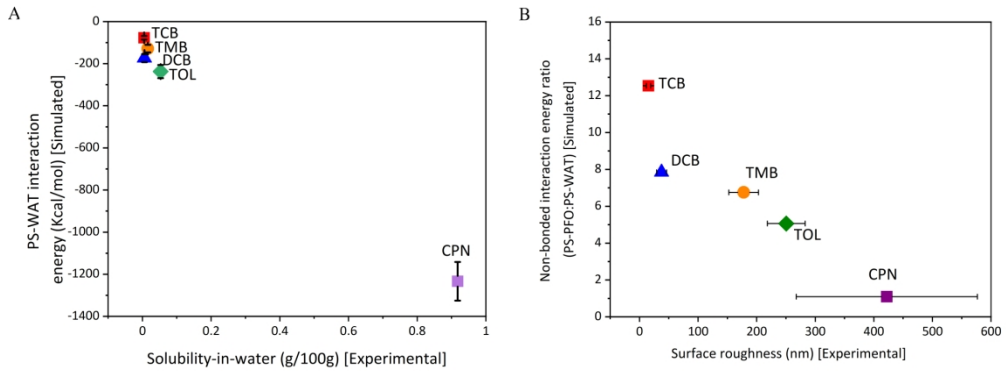

Figure 4 Correlation between simulated and experimental data for each primary solvent; (A) relation between simulated primary solvent-water (PS-WAT) interaction energy and experimental solubility-in-water value of primary solvents; (B) relation between simulated interaction energy ratio of primary solvent-polymer (PS-PFO) to primary solvent-water (PS-WAT) and experimental surface roughness of the film.

232x86mm (236 x 236 DPI)